Journal of Energy Storage 79 (2024) 109948

Contents lists available at ScienceDirect

Journal of Energy Storage

journal homepage: www.elsevier.com/locate/est

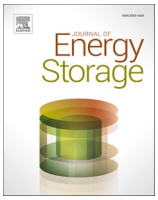

Research papers

Charging and discharging heat transfer improvement of shell-tube storage utilizing a partial layer of anisotropic metal foam

Mohamed Bouzidi [a,b], Mikhail Sheremet [c], Kyle Shank [d,e], Saeed Tiari [d], Mohammad Ghalambaz [c,*]

[a] Department of Physics, College of Science, University of Ha'il, P.O. Box 2440, Ha'il, Saudi Arabia
[b] Laboratoire de recherche sur les Hétéro-Epitaxies et Applications (LRHEA), Faculté des Sciences de Monastir, Université de Monastir, 5000 Monastir, Tunisia
[c] Laboratory on Convective Heat and Mass Transfer, Tomsk State University, Tomsk, Russia
[d] Biomedical, Industrial and Systems Engineering Department, Gannon University, 109 University Square, PA 16541, USA
[e] Mechanical Engineering Department, Gannon University, 109 University Square, PA 16541, USA

ARTICLE INFO

Keywords:
Anisotropic metal foam
Latent heat
Thermal energy storage
Metal foam
Heterogeneous angle

ABSTRACT

Latent heat thermal energy storage systems with phase change material are an efficient method to address the variability of renewable energy sources. Despite the prospect of the energy storge systems, the low thermal conductivity of phase change material is their main drawback, which hinders the thermal performance of the system. Recent studies have focused on the use of partial metal foam to increase the thermal response of the system; however, to the author's best knowledge, none of these investigations utilized a partial layer of anisotropic metal foam with tailored local characteristics to improve the heat transfer rate further. The present work investigates the application of an anisotropic layer of metal foam in an energy storage system to improve heat transfer and thermal energy storage rates. Heterogeneous copper metal foam is integrated into a shell-tube energy storage system with paraffin wax. The finite element method was applied to solve the governing equations coupled. Cases with various heterogenicity angles ranging from −90° to 90° in 15° increments are compared to a case with uniform foam. The cases are compared based on melting and solidification time, as well as the system energy response. The uniform foam case was charged and discharged in 646 and 1007 min. The most effective case in comparison was 0° heterogenicity angle with a charging and discharging time of 623 and 989 min, respectively.

1. Introduction

Phase change materials (PCMs) can store thermal energy by undergoing a phase shift between solid-liquid or liquid-gas. Most frequently, solid-liquid phase transitions are chosen due to relatively small volume changes. This feature makes them a desirable alternative for thermal energy storage (TES), especially when size and weight constraints render conventional storage technologies unfeasible [1,2]. A significant benefit of PCMs is their capacity to store high quantities of thermal energy in a small space, which makes them ideal for application in compact devices and systems. The ability of PCMs to maintain a constant temperature during phase transition makes them excellent for applications requiring isothermal conditions, such as building heating [3,4] or nano-coolant liquids [5–7].

Latent heat thermal energy storage (LHTES) is the technique of using PCM to store thermal energy. The PCM absorbs heat and undergoes a phase change from a solidus to a molten state during the charging process, storing energy in the material. When the stored energy is needed, the PCM is permitted to undergo a phase shift in the opposite direction, releasing the thermal energy [8,9]. LHTES systems offer a wide variety of applications, including storing surplus energy during peak production times for subsequent usage in renewable energy systems such as solar power plants and waste heat recovery [10,11]. They may also be utilized in household and commercial heating and cooling systems [12], as well as in industrial applications such as the storage and transportation of food products [13].

One of the primary obstacles to the widespread use of PCMs and LHTES systems is their poor thermal conductivity compared to

* Corresponding author.
E-mail addresses: m.bouzidi@uoh.edu.sa (M. Bouzidi), sheremet@math.tsu.ru (M. Sheremet), shank003@gannon.edu (K. Shank), tiari001@gannon.edu (S. Tiari), m.ghalambaz@gmail.com (M. Ghalambaz).

https://doi.org/10.1016/j.est.2023.109948
Received 16 May 2023; Received in revised form 23 November 2023; Accepted 2 December 2023
Available online 23 December 2023

conventional storage materials, which may result in inefficient heat transfer [14]. However, current research focuses on creating novel materials and enhancing system design to increase the efficiency and efficacy of these systems. One approach for enhancing heat transfer is embedding the PCM in a highly thermally conductive metal foam [15,16]. Porous materials and open-cell metal foams are being investigated increasingly as a technique to improve the heat transfer properties of PCMs [15,17].

Porous materials are distinguished by their capacity to enable fluids to pass through them, which may increase the available surface area for heat transfer. This characteristic makes them well suited for use as a medium for PCMs, since they may offer a vast surface area for the PCM to come into contact with, facilitating effective heat transfer. This role is served by porous materials such as expanded graphite [18], silica aerogel [19], and cellulose-based polymers [20].

Metal foams with open cells are another promising material for increasing heat transfer in PCMs. These foams consist of an interconnected network of metallic struts or pores, which may offer a huge surface area for heat transfer [21]. The open cell form also facilitates fluid movement, which promotes efficient heat transfer [22]. Metal foams with open cells have been used in various applications, including solar LHTES systems [23] and electronic cooling systems [24,25].

It is feasible to increase the performance and efficiency of LHTES systems by combining porous materials and open-cell metal foams [26]. By increasing the accessible surface area for heat transfer, these materials may assist in minimizing the time necessary for charging and discharging the PCM while enhancing the system's total energy storage capacity. As research continues in this field, these materials are anticipated to be further developed and optimized for TES applications.

In the realm of heat transfer applications, recent researchers have shown interest in anisotropic porous structures [27,28]. Metal foams are a revolutionary method for increasing the heat transfer rate to and from PCMs for applications involving LHTES [29].

Few literature studies considered the heat transfer of anisotropic porous materials with no phase change involvement. Rashed et al. [30] used Buongiorno's nonhomogeneous two-phase nanofluids model to examine convection in cubic enclosures filled with homogeneous or heterogeneous porous media with changing permeability and thermal conductivity. An Al_2O_3-water nanofluid with changeable properties was used. It was reported that heterogeneous permeability in all directions had the greatest average Nusselt number, while the homogeneous instance had the lowest heat transfer rate. In addition, the research indicated that raising the Rayleigh and Darcy numbers enhanced the average Nusselt number for all porous situations examined. Heterogeneous permeability in both directions produced the greatest average Nusselt number, while uniform porosity had the lowest.

Maghsoudi and Siavashi [31] improved the mixed convection of Cu-water nanofluid in a two-sided, lid-driven cavity containing heterogeneous porous media. A two-phase mixture model and the Darcy-Brinkman-Forchheimer relation were used to simulate the nanofluid and fluid flow. To optimize the average Nusselt number for varied Rayleigh and Richardson numbers, the optimization procedure evaluated pore size diameters in various cavity parts as choice factors. The research aimed to develop a heterogeneous porous medium with a higher average Nusselt than the homogeneous medium with the greatest Nusselt. According to the findings, the adjusted heterogeneous porous medium boosted heat transfer by up to 8.3 % for convection-dominant flows. Nonetheless, the optimum porous medium for natural convection-dominated flows was the homogeneous porous instance with the largest pore diameter. At optimum circumstances, the drag force on the driven lid rose by a minimal 0.34 %.

The convective flow of a power-law nanofluid inside a cubic enclosure filled with a heat-generating and 3D-heterogeneous porous medium was investigated using the 3D-SIMPLE technique of the finite volume method [32]. The authors examined a heterogeneous porous medium at three levels and tested three power-law indices. The maximum temperature increased in Newtonian fluid and homogenous porous material. Another study [33] showed that heterogeneity significantly impacts the total entropy generation in permeability. The Marangoni number becomes a more influential parameter on the total entropy production at lower Rayleigh numbers. In addition, the power-law index has a major impact on the flow field and the formation of entropy [34].

The accuracy of the Fourier-Galerkin technique for natural convection in a square enclosure containing a heterogeneous porous media is studied in [35]. New research casts doubt on the accuracy of the low-resolution porous-continuum model used to simulate natural convection in enclosures containing discrete solid blocks [36]. In order to verify the results, they are compared to a continuum model in which equilibrium equations are solved for each component, and compatibility requirements are applied to their interfaces. The porous–continuum model is a more straightforward mathematical model; however, it is limited to situations in which the transport phenomena permit homogeneity of the domain. More research is required to assess the porous-continuum model accuracy for heterogeneous structures.

Considering the PCM and anisotropic metal foams, Shafi et al. [37] recently utilized a high-porosity anisotropic copper metal foam filled with RT-82 PCM for LHTES in a shell-tube unit. The unit was fully filled with metal foam, and an anisotropic porous media modeled the composite metal foam. A neural network model was trained with 4998 data samples to find a map between design parameters and the PCM melting. The anisotropy angle affected the energy storage rate, with an angle of fewer than 45° producing the highest storage rate. An optimal anisotropic angle might cut melting time by approximately 7 % without raising the weight or affecting the unit storage capacity.

Several recent publications investigated the use of PCMs in shell-tube LHTES units. Cui et al. [38] provided an excellent review on the placement of metal foams filled with PCMs in LHTES units. Nedjem et al. [39] explored the combination of several heat transfer strategies in a triplex tube to increase the efficiency of the LHTES system with paraffin PCM. Models investigated the TES effects of uniform and non-uniform fins, fins-nanoparticles, and fins-metal foam. The predictions that non-uniform fin configurations would increase melting rates by 56.45 % were supported by experimental results. Fins-metal foam increases heat transfer compared to fins-nanoparticles, lowering complete discharging and charging times by up to 90.04 % and 80.12 %, respectively.

Fins and metal foam are often combined with PCMs to increase their thermal conductivity in LHTES systems. Yet, comparable analyses of these methods during the phase transition are uncommon. Joshi and Rathod [40] analyzed the thermal performance of fins and metal foam-infused LHTES systems with the same variables of compactness. Compared to pure stearic acid PCM, the findings indicate that fins and metal foam improve melting and solidification heat transfer rates by 50 % and 16.67 % and 5.56 %, and 33.33 %, respectively. In terms of overall cycle time, metal foam performs better, although fins increase melting rates more.

A novel LHTES unit has been developed using metal foams with varying pore characteristics to enhance performance by Yang et al. [41]. Positive and negative porosity, pore density gradients, and physical and numerical models were constructed. An experimental test apparatus was used to validate the numerical model. The positive porosity gradient reduced the complete melting time by 17.9 % and improved temperature uniformity compared to a uniform porosity case. The optimization suggested a porosity gradient of 0.89–0.95-0.98 to minimize melting time by an additional 21.1 %.

Prior research [39,40,42,43] has investigated the usage of partial metal foams to improve the TES rate of shell-tube shape LHTES units. To the authors' best knowledge, none of these investigations have utilized a partial layer of anisotropic metal foam with tailored local characteristics to improve the energy storage rate further. The present work proposes to investigate the application of an anisotropic layer of metal foam in a shell-tube LHTES system to improve heat transfer and TES rates. By integrating an anisotropic layer with unique local properties, the study

intends to increase the LHTES unit performance, allowing for more efficient TES and heat transfer. The findings of this study could have significant ramifications for the design of LHTES systems, leading to the creation of more efficient and effective systems for various industrial and domestic applications.

2. Model description

LHTES is a key feature in developing solar energy technologies because solar energy is an inherently fluctuating energy source depending on weather and time of day. LHTES systems have the capability to store a substantial quantity of thermal energy at a fusion temperature within a compact volume. Thus, it compensates for energy fluxes in transient solar energy systems. For example, in Fig. 1. a schematic view of a concentrated-solar heating system for building heating is illustrated. This solar energy system includes a solar collector, a storage tank, an LHTES unit, and circulating pumps. The concentrated solar collector heats the water and stores it in the form of sensible heat in the hot water tank. The tank supplies the hot water to the building on demand. The hot water tank is connected to the LHTES unit through an auxiliary cycle. When there is a low energy demand by building or extensive energy generation in solar collectors, the pump in the auxiliary energy storage loop activates and dumps its excess heat into the LHTES unit when there is excessive energy generation in the collectors. The tank can also withdraw energy from the LHTES unit when solar energy generation is not enough.

In the present study, an LHTES unit is made with a shell-tube structure as depicted in Fig. 2. A heat transfer fluid (HTF), water, with a gauge pressure P_{in} enters the tube and exists the top port with a zero relative pressure. The HTF tube is made of copper with a thickness of t and external radius R. There is a partial layer of heterogeneous metal foam made of copper over the HTF tube inside the shell. After the foam layer, there is a void space between the metal foam layer and the shell wall. The shell domain, including the foam layer and the void space, is filled by paraffin wax which acts as the PCM which can store/release the latent heat energy at a fusion temperature of T_f.

The water enters the HTF tube at a uniform temperature T_{in} and begins transferring thermal energy to the PCM through the tube wall. Then, water leaves the tube at an elevated or reduced temperature depending on the discharging/charging process. Several LHTES units can be added to the system in various arrangements [44,45], such as parallel, series, or hybrid arrangements, to cover the required capacity and demands of the cycle depicted in Fig. 1. Here, the aim is to analyze the heat transfer design of an LHTES unit incorporating a heterogeneous foam layer.

In LHTES units, the low thermal conductivity of PCMs is a significant barrier to energy storage/release rate. An LHTES should quickly react to the energy demands of the hot tank. Thus, here, a heterogeneous foam layer was added to the unit to enhance the heat transfer rate and response time of the unit. The hot tank dumps the excess thermal energy to the LHTES unit at set point temperature $T_h = T_f + 15\ ^\circ C$ when the unit is at an initial temperature $T_0 = T_f$-15 °C. Thus, T_h can be considered as

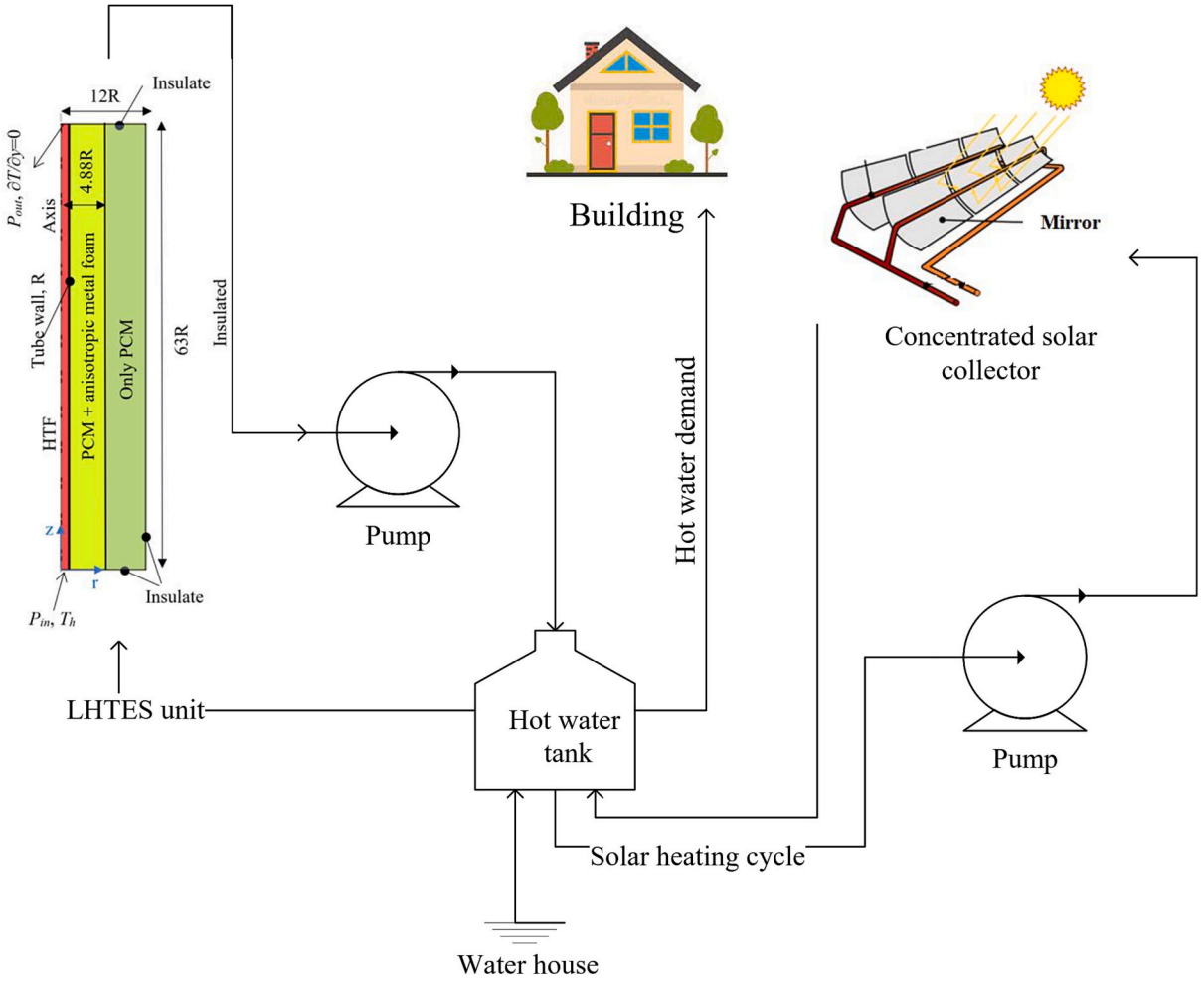

Fig. 1. A schematic diagram of a concentrated-solar heating system for building heating consisting of a solar collector, a storage tank, an LHTES unit, and circulating pumps.

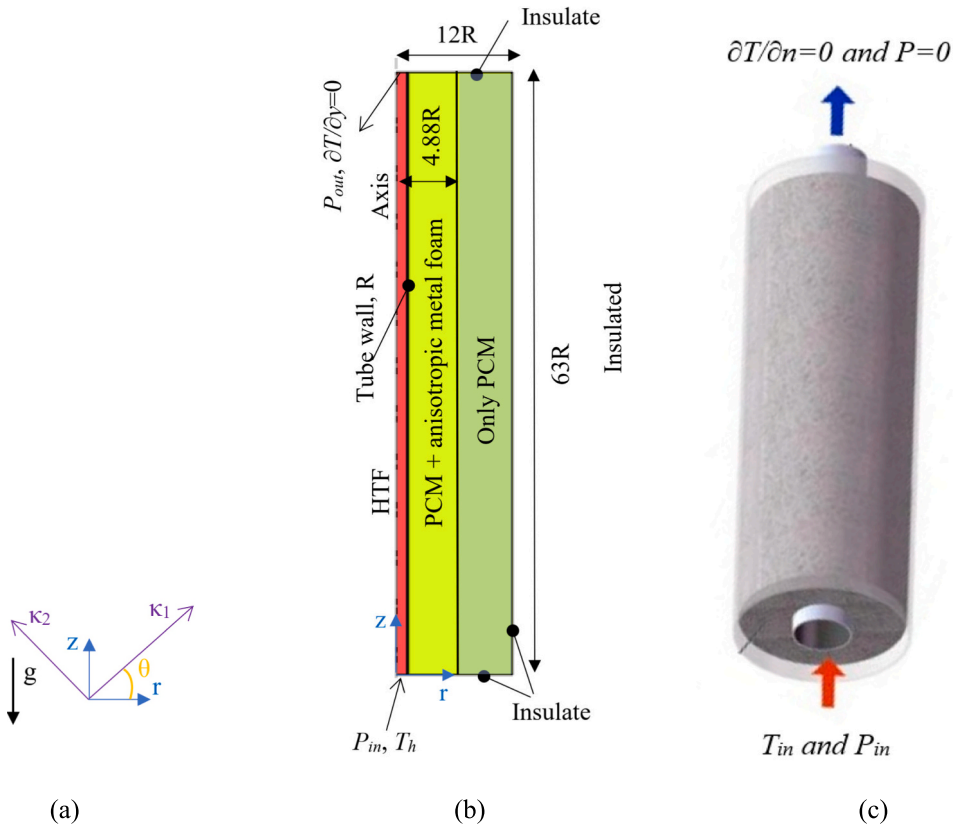

Fig. 2. The physical model of the shell-tube storage filled by a layer of anisotropic metal foam. (a) the applied coordinate system and the anisotropic angles; (b) An axis-symmetric two-dimensional representation of the storage model; (c) A full three-dimensional representation of the model with inlet and outlet HTF boundary conditions.

the inlet temperature of HTF, $T_{in} = T_h$, during the charging process. The hot tank withdraws energy from the LHTES at a set point of $T_C = T_f$-15 °C from a charged unit at an initial temperature $T_0 = T_f + 15$ °C.

2.1. Principal equations

The physical model comprises three distinct regions: the HTF, the copper tube wall, and the composite metal foam-phase change material (MF-PCM). These regions are physically interconnected. The governing equation in a cylindrical coordinate system pertains to heat conduction transfer in the copper wall and can be articulated as:

$$(\rho C_p)_{Wall}\frac{\partial T}{\partial t} = k_{Wall}\left(\frac{\partial^2 T}{\partial z^2}+\frac{1}{r}\frac{\partial}{\partial r}\left(r\frac{\partial T}{\partial r}\right)\right) \quad (1)$$

Here, C_p, ρ, and k denote the specific heat capacity, density, and thermal conductivity of the tube wall, respectively. Additionally, T and t signify the temperature field and time correspondingly. The r- and z-axis introduce the cylindrical coordinate system, as demonstrated in Fig. 2, with the "wall" subscript representing the shell. For the HTF region, the governing equations encompass continuity, momentum, and energy:

$$\frac{1}{r}\frac{\partial(ru_r)}{\partial r}+\frac{\partial u_z}{\partial z} = 0 \quad (2)$$

$$\rho_{HTF}\left(\frac{\partial u_r}{\partial t}+u_z\frac{\partial u_r}{\partial z}+u_r\frac{\partial u_r}{\partial r}\right) = -\frac{\partial p}{\partial r}+\frac{\mu_{HTF}}{r}\frac{\partial}{\partial r}\left(r\frac{\partial u_r}{\partial r}\right)+\mu_{HTF}\frac{\partial^2 u_r}{\partial z^2}-\frac{\mu_{HTF}u_r}{r^2} \quad (3\text{-a})$$

$$\rho_{HTF}\left(\frac{\partial u_z}{\partial t}+u_z\frac{\partial u_z}{\partial z}+u_r\frac{\partial u_z}{\partial r}\right) = -\frac{\partial p}{\partial z}+\frac{\mu_{HTF}}{r}\frac{\partial}{\partial r}\left(r\frac{\partial u_z}{\partial r}\right)+\mu_{HTF}\frac{\partial^2 u_z}{\partial z^2} \quad (3\text{-b})$$

$$(\rho C_p)_{HTF}\left(\frac{\partial T}{\partial t}+u_z\frac{\partial T}{\partial z}+u_r\frac{\partial T}{\partial r}\right) = k_{HTF}\left(\frac{1}{r}\frac{\partial}{\partial r}\left(r\frac{\partial T}{\partial r}\right)+\frac{\partial^2 T}{\partial z^2}\right) \quad (4)$$

In this case, u_r and u_z denote the velocity components in the radial and axial directions. The subscript HTF signifies the HTF, and the dynamic viscosity is symbolized by μ. Furthermore, the HTF flow was considered laminar (Re_{HTF} ⟨2000) with fixed properties. The Reynolds number is introduced based on the tube diameter as $Re_{HTF} = \rho_{HTF} \times u \times D/\mu_{HTF}$ and $u = \sqrt{(u_r^2 + u_z^2)}$. It is important to note that gravity effects were neglected in the HTF since a forced convection flow operates in a closed loop.

The open cells' metal foam allows the molten PCM to flow within the pores. Due to temperature gradients in the molten PCM, buoyancy forces may trigger natural convection flow circulation. Hence, it is necessary to solve the flow and phase change heat equations in the PCM domain. The phase change is modeled by the enthalpy porosity approach, which tracks the melt fraction in the domain. A local-thermal non-equilibrium (LTNE) approach was employed to make a distinction between the MF and PCM temperatures. Further mode, the non-Darcy effects were also considered. Thus, the differential equations representing the physical model are expressed [46–48]:

$$\frac{1}{r}\frac{\partial(ru_r)}{\partial r}+\frac{\partial u_z}{\partial z} = 0 \quad (5)$$

$$\frac{\rho_{PCM}}{\varepsilon}\left(\frac{\partial u_r}{\partial t}+\frac{1}{\varepsilon}\left(u_z\frac{\partial u_r}{\partial z}+u_r\frac{\partial u_r}{\partial r}\right)\right) = -\frac{\partial p}{\partial r}+\frac{\mu_{PCM}}{\varepsilon}\left[\frac{1}{r}\frac{\partial}{\partial r}\left(r\frac{\partial u_r}{\partial r}\right)-\frac{u_r}{r^2}+\frac{\partial^2 u_r}{\partial z^2}\right] -\rho_{PCM}\frac{C_F}{\sqrt{\kappa}}|u|u_r+A_{mush}\frac{(1-\varphi(T))^2}{\lambda_{mush}+\varphi^3(T)}u_r-\frac{\mu_{PCM}}{\kappa}u_r \quad (6\text{-a})$$

$$\frac{\rho_{\mathrm{PCM}}}{\varepsilon}\left(\frac{\partial u_z}{\partial t}+\frac{1}{\varepsilon}\left(u_z\frac{\partial u_z}{\partial z}+u_r\frac{\partial u_z}{\partial r}\right)\right)=-\frac{\partial p}{\partial z}+\frac{\mu_{\mathrm{PCM}}}{\varepsilon}\left[\frac{\partial^2 u_z}{\partial z^2}+\frac{1}{r}\frac{\partial}{\partial r}\left(r\frac{\partial u_z}{\partial z}\right)\right]$$
$$-\rho_{\mathrm{PCM}}\frac{C_F}{\sqrt{\kappa}}|u|u_z+A_{mush}\frac{(1-\varphi(T))^2}{\lambda_{mush}+\varphi^3(T)}u_z-\frac{\mu_{\mathrm{PCM}}}{\kappa}u_z+g\rho_{\mathrm{PCM}}\beta_{\mathrm{PCM}}(T-T_0) \quad (6\text{-b})$$

$$(\rho C_p)_{\mathrm{PCM}}\left(\varepsilon\frac{\partial T_{\mathrm{PCM}}}{\partial t}+\left(u_z\frac{\partial T_{\mathrm{PCM}}}{\partial z}+u_r\frac{\partial T_{\mathrm{PCM}}}{\partial r}\right)\right)=$$
$$\frac{1}{r}\frac{\partial}{\partial r}\left(k_{\mathrm{eff,PCM}}r\frac{\partial T_{\mathrm{PCM}}}{\partial r}\right)+\frac{\partial}{\partial z}\left(k_{\mathrm{eff,PCM}}\frac{\partial T_{\mathrm{PCM}}}{\partial z}\right)-\varepsilon\rho_{\mathrm{PCM}}L_{\mathrm{PCM}}\frac{\partial\varphi(T)}{\partial t}+h_v(T_{\mathrm{MF}}-T_{\mathrm{PCM}}) \quad (7\text{-a})$$

$$(\rho C_p)_{\mathrm{MF}}(1-\varepsilon)\frac{\partial T_{\mathrm{MF}}}{\partial t}=\frac{1}{r}\frac{\partial}{\partial r}\left(k_{\mathrm{eff,MF}}r\frac{\partial T_{\mathrm{MF}}}{\partial r}\right)+\frac{\partial}{\partial z}\left(k_{\mathrm{eff,MF}}\frac{\partial T_{\mathrm{MF}}}{\partial z}\right)-h_v(T_{\mathrm{MF}}-T_{\mathrm{PCM}}) \quad (7\text{-b})$$

Here, κ and C_F represent the porous permeability and Frochheimer parameters, respectively. The heat transfer between the PCM inside the pores and the porous matrix is taken into account using h_v as the volumetric heat transfer coefficient, which will be introduced in detail later. The effective properties (eff) and metal foam (MF) are introduced with the corresponding subscripts. The symbols L, β, and g stand for the latent heat of fusion, thermal volume expansion coefficient, and gravity acceleration, respectively. Two parameters A_{mush} and λ_{mush} are adopted with large ($A_{\mathrm{mush}} = 10^{10}$ Pa.s/m^2) and small values ($\lambda_{\mathrm{mush}} = 0.001$) to keep the velocity components insignificant on the solid PCM regions. Furthermore, a linear artificial dynamic viscosity is applied for better convergence as $\mu_{\mathrm{PCM}} = (1\text{-}\varphi) \times \mu_{\mathrm{a}} + \varphi \times \mu_{\mathrm{PCM,l}}$, where the artificial viscosity $\mu_{\mathrm{a}} = 10^4$ Pa.s [37]. Besides, $|u| = \mathrm{sqrt}(u_z^2 + u_r^2)$.

Eqs. (7-a) and (7-b) illustrate heat transfer within the MF and PCM phases. The term h_v accounts for the thermal interplay between the two phases. In these equations, the effective thermal conductivities for MF and PCM are utilized, as pore structures directly impact these thermal conductivities [49]. The PCM temperature drives the melting volume fraction, φ, as follows [50]:

$$\varphi(T)=\begin{cases}0 & T<T_{\mathrm{f}}-\frac{1}{2}\Delta T_{\mathrm{f}}\ \text{(Solidous phase)}\\ \frac{(T-T_{\mathrm{f}})}{\Delta T_{\mathrm{f}}}+\frac{1}{2} & T_{\mathrm{f}}-\frac{1}{2}\Delta T_{\mathrm{f}}\le T\le T_{\mathrm{f}}+\frac{1}{2}\Delta T_{\mathrm{f}}\ \text{(Solidous-Liquid region)}\\ 1 & T>T_{\mathrm{f}}+\frac{1}{2}\Delta T_{\mathrm{f}}\ \text{(Liquid phase)}\end{cases} \quad (8)$$

Here, ΔT_{f} represents the phase transition interval surrounding the fusion temperature, T_{f}. The governing equations take into consideration the average permeability (κ_{a}) and porosity (ε_0) of both the foam layer and the clear fluid region:

$$\text{In clear region (no metal foam)}: \quad \varepsilon = 1 \ \text{ and } \kappa\to\infty \quad (9a)$$

$$\text{In metal foam region}: \varepsilon=\varepsilon_0, \ \ \kappa=\kappa_a \quad (9b)$$

Anisotropic foams have a directionally dependent structure, meaning that the structure of the foam is optimized in certain local directions to improve local heat conductivity and permeability [51]. This method is especially valuable in LHTES applications, where heat transfer performance is crucial to the system's efficacy and efficiency. Anisotropic metal foams enable more control over the flow of heat through the material, facilitating more efficient heat transfer. The anisotropic nature of MF thermal conductivity and permeability allows for changes in principal directions. By reinforcing ligaments of MF in a principal direction, thermal conductivity is enhanced at the expense of decreased permeability. Consequently, a second-order tensor is employed to introduce these properties [52]:

$$\kappa=\begin{bmatrix}\kappa_1(cos\theta)^2+\kappa_2(sin\theta)^2 & (\kappa_1-\kappa_2)sin\theta cos\theta\\ (\kappa_1-\kappa_2)sin\theta cos\theta & \kappa_1(sin\theta)^2+\kappa_2(cos\theta)^2\end{bmatrix} \quad (10\text{-a})$$

$$k_{\mathrm{eff,MF}}=\begin{bmatrix}k_1(cos\theta)^2+k_2(sin\theta)^2 & (k_1-k_2)cos\theta sin\theta\\ (k_1-k_2)cos\theta sin\theta & k_1(sin\theta)^2+k_2(cos\theta)^2\end{bmatrix} \quad (10\text{-b})$$

The values $\kappa_1 = \kappa_{\mathrm{a}} \times (1-K_n)$, $k_1 = k_{\mathrm{a}} \times (1 + K_n)$, $\kappa_2 = \kappa_{\mathrm{a}} \times (1 + K_n)$, and $k_2 = k_{\mathrm{a}} \times (1 - K_n)$ represent the anisotropic properties. The anisotropic angle (θ) is delineated in Fig. 2(b) and exemplifies the anisotropic angle positioning within the cavity. The anisotropic factor (K_n) is employed here, with $K_n = 0$ indicating isotropic MF. The MF must remain interconnected and continuous, thus preventing K_n from being excessively high. Here, k_{a} denotes the effective thermal conductivity of MF. In practical terms, the heterogeneous metal foam can initially be fabricated in an orthogonal direction, resulting in a zero anisotropic angle ($\theta = 0°$). Subsequently, the created heterogeneous metal foam can be rotated and sectioned in any desired direction. The anisotropic angle (θ) is then defined as the angle between the orthogonal direction and the orientation of the metal foam, as illustrated in Fig. 2(b).

In this study, a moderate anisotropic factor of $K_{\mathrm{n}} = 0.2$ is adopted [48]. The average permeability (κ_{a}) [53] and metal foam's average effective thermal conductivity (k_{a}) is calculated with the following formulas [46,49]:

$$k_a=\frac{(1-\varepsilon)}{3}k_{\mathrm{MF}} \quad (11)$$

$$\kappa_a=\frac{\varepsilon^2}{36}\frac{\left(\sqrt{\frac{\kappa_{tor}}{3\varepsilon}}d_{fp}\right)^2}{\kappa_{tor}(\kappa_{tor}-1)} \quad (12)$$

In these equations, k_{MF} represents the MF's bulk thermal conductivity, while d_{fp} and κ_{tor} are introduced as follows [53]:

$$d_{fs}=1.18\left\{\frac{1}{1-e^{\frac{(\varepsilon-1)}{0.04}}}\right\}\sqrt{\frac{(1-\varepsilon)}{3\pi}}d_{fp} \quad (13)$$

$$\frac{1}{\kappa_{tor}}=\frac{1}{\varepsilon}\left[\frac{3}{4}+\frac{\sqrt{9-8\varepsilon}}{2}cos\left\{\frac{4}{3}\pi+\frac{1}{3}cos^{-1}\left(\frac{8\varepsilon^2+27-36\varepsilon}{(9-8\varepsilon)^{\frac{3}{2}}}\right)\right\}\right]d_{fp} \quad (14)$$

In this case, d_{fp} is determined using the pore per inch (PPI) property of the MF [53]:

$$d_{fp}=2.54\times10^{-2}/PPI \quad (15)$$

The Frochheimer parameter is computed using the given equation [53]:

$$C_F=0.00212\times\left(\frac{d_{fs}}{d_{fp}}\right)^{-1.63}(1-\varepsilon)^{-0.132} \quad (16)$$

The study performed in [54] introduces h_v as a function of the Nusselt

number:

$$h_v = \frac{k_{\mathrm{PCM}}}{d_{fs}^2} Nu_v \tag{17}$$

where Nu_v is defined in the volumetric form. Here, Nu_v is calculated for low pore scale Reynold numbers as follows [54]:

$$Nu_v = \begin{cases} 76.99 - 152.01 \times \varepsilon + 75.04 \times \varepsilon^2 & 0 \le Re \le 0.1 \\ \left(1.72 + 1.71 \times \varepsilon - 3.46 \times \varepsilon^2\right) \times Re^{0.26} \times Pr^{0.28} & 0.1 < Re \le 1 \end{cases} \tag{18}$$

In this context, $\alpha_{\mathrm{PCM}} = k_{\mathrm{PCM}}/(\rho C_p)_{\mathrm{PCM}}$ and $\mathrm{Pr} = \mu_{\mathrm{PCM}} \times \rho_{\mathrm{PCM}}/\alpha_{\mathrm{PCM}}$. The Reynolds number ($Re$), at the pore scale, is computed as $Re = d_{fs} \times |u|_{\mathrm{PCM}} \times \rho_{\mathrm{PCM}}/\mu_{\mathrm{PCM}}$. This relation is in good agreement with the zero or small velocities of PCM in metal foam [37].

In conclusion, $k_{\mathrm{eff,PCM}}$ was assessed using the following references [46, 49]. To calculate the thermophysical properties within the phase change interface, a linear weight average was employed:

$$k_{\mathrm{eff,PCM}} = k_{\mathrm{PCM}} \frac{\varepsilon + 2}{3} \tag{19}$$

$$\left(\rho C_p\right)_{\mathrm{PCM}} = \varphi\left(\rho C_p\right)_{\mathrm{s}} + (1-\varphi)\left(\rho C_p\right)_{\mathrm{l}} \tag{20}$$

$$\rho_{\mathrm{PCM}} = \varphi\rho_{\mathrm{s}} + (1-\varphi)\rho_{\mathrm{l}} \tag{21}$$

In this case, the subscripts are used to indicate the solid-PCM (s) and the liquid-PCM (l). Table 1 provides a summary of the properties of the paraffin, MF, and tube.

2.2. Initial and boundary conditions

The continuity of the heat flux and the temperature were applied to interconnected walls. The continuity of temperature was also employed when there was LTNE, while the heat flux (q) continuity was split between the porous and PCM phases as [37]:

$$q_{\mathrm{Wall}} = (1-\varepsilon) q_{\mathrm{PCM}} + \varepsilon q_{\mathrm{MF}} \tag{22}$$

A consistent inlet temperature of T_{h} was employed, with T_{h} set at 65.5 °C. The HTF inlet port is subject to a gauge pressure P_{in}. The LHTES unit was presupposed to commence with a temperature of $T_{\mathrm{c}} = 36.5$ °C. The boundary surfaces were all treated with no-slip and impermeability conditions, with the exception of the boundaries for the inlet and outlet, which had already been delineated. The lower left corner of the shell space was assigned a pressure reference [37]. The walls of the shell were considered thoroughly insulated. The outlet encountered a condition of the outflow with a relative pressure of zero and -n.q = 0, where 'n' symbolizes the normal vector to a surface.

2.3. Key parameters

The MVF represents the average quantity of liquefied PCM and is evaluated as:

$$MVF = \oint_V \varphi \varepsilon dV \Big/ \oint_V \varepsilon dV \tag{23}$$

Here, V is the PCM domain, and dV denotes the volumetric element. The thermal energy accumulation is calculated as the summation of latent and sensible heat:

$$\begin{aligned} Q_{sensible} = {} & (\rho C_P)_{\mathrm{MF}}(T - T_0) \oint_V (1-\varepsilon) dV \\ & + \left[\oint_V \left(\int_{T_0}^{T} (\rho C_P)_{\mathrm{PCM}}(T) \varepsilon dT \right) dV \right] \\ & + (\rho C_P)_{\mathrm{Wall}} V_{\mathrm{Wall}}(T - T_0) + (\rho C_P)_{\mathrm{HTF}} V_{\mathrm{HTF}}(T - T_0) \end{aligned} \tag{24}$$

$$Q_{latent} = \varepsilon \oint_V L_{\mathrm{PCM}} \rho_{\mathrm{PCM}} \varphi dV \tag{25}$$

$$Q_{\mathrm{store}} = Q_{\mathrm{latent}} + Q_{\mathrm{sensible}} \tag{26}$$

Energy Storage Power is computed as.

$$\mathrm{Power} = Q_{\mathrm{store}}/t \tag{28}$$

3. Numerical method and model evaluation

The details of the numerical method, mesh sensitivity analysis, and model evaluations are reported in this section.

3.1. Finite element method

The control equations, along with their initial and boundary conditions, were solved using the finite element method (FEM) to adequately address the nonlinear sink/source terms resulting from phase transitions [60,61]. By transforming the governing equations into their weak form and adopting a second-order discretization for heat and momentum equations, an algebraic set of residual equations was obtained through Gauss quadrature integration over elements. The residual equations were solved iteratively in a coupled manner using the Newton method [62,63] with a damping factor of 0.8 to enhance convergence. The PARDISO parallel solver with the Newton method was employed to handle the computations in parallel using multiple CPU cores [64,65]. The solution time steps and convergence were automatically regulated to maintain the relative solution accuracy below 10E-4 using the first-second order backward differential formula (BDF) [66].

FEM provided a continuous, accurate, and smooth result over the discretized mesh, appropriate for the purpose of the current research. The computations were initiated with the initial conditions and continued to investigate the energy storage and phase change behavior. At the onset of each simulation, the anisotropic angle (θ) was established as a constant. Corresponding thermophysical properties, including effective thermal conductivity and permeability for the metal foam in the x and y directions, were subsequently calculated. These determined properties were then integrated into the governing equations as two-dimensional tensors.

The heat and continuity equations along with the phase field variable terms (φ), were considered fully-coupled and solved iteratively. Computation was designed to cease when a fully melted state was achieved, indicated by an MVF of ≥0.999 or higher, serving as the termination criteria.

The fluid flow in the HTF tube was obtained in a steady-state phase, given the independence from the HTF flow from the LHTES unit's thermal operating conditions. Subsequently, the calculated velocity components were incorporated as unchanging initial values in simulations, reducing computational costs without affecting the simulation results. A flowchart outlining the applied computational algorithm is

Table 1
A Summary of the thermophysical characteristics for involved material.

Materials	ρ (kg/m^3)	k (W/m.K)	C_p (J/kg.K)	T_m (°C)	L (kJ/kg)	μ (kg/m.s)	β (1/K)
Paraffin (solid/liquid) [55–57]	916/790	0.21/0.12	2700/2900	49–54	176	0.0036	0.00091
Water [58]	997.1	0.613	4179	–	–	0.000957	0.00021
Copper foam [59]	8900	380	386	–	–	–	–

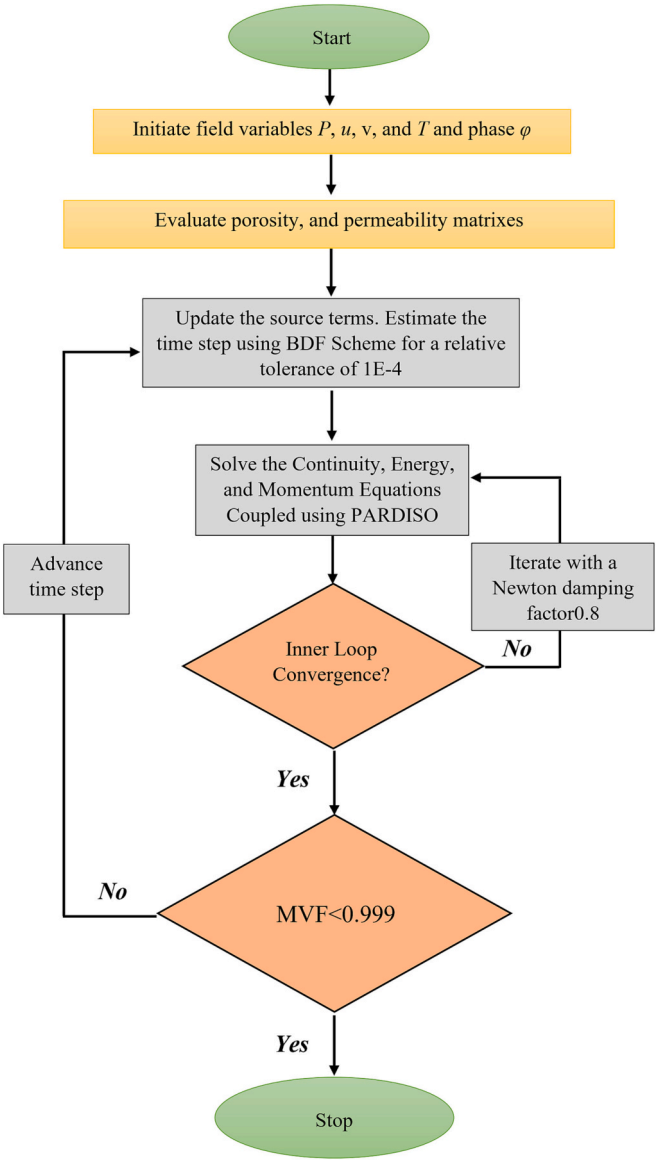

Fig. 3. Flowchart of the applied numerical method for solving the governing equations.

Table 2
Details of mesh cases as a function of mesh control parameter *Nm*.

Nm	Tube wall	HTF width	Height	PCM width	Melting computational time (hours)	Solidification computational time (hours)
2	2 × *Nm*	10 × *Nm*	45 × *Nm*	30 × *Nm*	27.1	1.4
3					54.1	4.0
4					80.2	4.5
5					107.2	12.0

provided in Fig. 3.

3.2. Grid resolution

The impact of grid resolution on the precision of numerical calculations was investigated by performing computations for a range of grid sizes. A case with $K_n = 0.2$, $\theta = 0°$, and $P_{in} = 10$ Pa was examined and solved using different grid resolutions controlled by *Nm* parameter. A structured mesh was applied to discretize the solution domain. A non-uniform mesh with a stretching factor 0.1 was applied in the HTF region, which is dense next to the tube wall, to better capture the velocity and temperature gradients. The values of *Nm* parameter are listed in Table 2. The calculated MVF during the solid-liquid phase change is illustrated in Fig. 4. The overlapping curves indicate the high level of accuracy achieved in the computations. It is important to mention that the time step was dynamically managed by the BDF method to maintain a relative tolerance below 0.0001. It was observed that utilizing a grid size with $Nm = 3$ led to a significant reduction in the necessary time step sizes, ensuring accurate calculations. However, this also resulted in an increase in the overall computational time. Consequently, a grid size of $Nm = 3$ was selected as a proper mesh to strike a balance between computational precision and efficiency. Fig. 5 shows a view of selected mesh with $Nm = 3$. Each distinct domain within the mesh is represented using a unique color to enhance clarity and readability.

3.3. Model validation and code verification

Fahs et al. [35] conducted a study examining natural convection flow and heat exchange within an anisotropic porous material characterized by a local thermal conductivity depending on material space coordinates. This gradient relied on a distribution variable, K_n, which is a parameter with almost similar function to K_n but with a logarithmic function distribution. Here, the same definition as indicated [35] for K_n was adopted for the sake of comparison. Moreover, in [35], only permeability was locally variable, and thermal conductivity was homogeneous.

In instances where K_n equaled 2.0, dimensionless temperatures from [35] were contrasted with the numerical findings of this current investigation, as depicted in Fig. 6. The results are provided for a case with permeability variation only in the *x* direction and uniform permeability in the *y* direction. The outcomes presented in Fig. 6 demonstrate a strong agreement between the present calculations and the prior research.

The accuracy and precision of the current numerical model and simulations were evaluated by comparing the results with experimental data from Kamkari et al. [67] and the theoretical findings of Kamkari and Amlashi [68]. In these studies, the melting of lauric acid PCM in a rectangular enclosure of dimensions 120 × 50 mm was examined, with the left vertical wall being isothermally heated at $T_h = 70$ °C while the other surfaces were well insulated. Kamkari et al. [67] employed a local thermal equilibrium model for their analysis.

The MVF was compared between the current study and the referenced literature works. As depicted in Fig. 7, the results demonstrate an acceptable agreement, confirming the correctness and accuracy of the simulations and the current model.

In relation to the melting process of composite paraffin wax and metal foam, the outcomes of the current computational model were evaluated against the experimental findings presented by Zheng et al. [59]. The melting event for the paraffin wax took place within a square chamber measuring 100 mm, with one of its vertical surfaces subjected to a continuous heat flux of 1150 W. A minor heat dissipation occurred from the sides of the enclosure. The copper metal foam had a porosity value of 0.95 and 5 PPI pores. Fig. 8 illustrates the melting boundary at heating intervals of 1.5, 3, and 4.5 h. The form and location of the interface, as determined by the present simulation, closely resemble the observations made in [59].

4. Results and discussion

The impact of the heterogeneous angle of the foam layer (θ) on the LHTES unit performance is addressed in this section. The value of inlet pressure was fixed at $P_{in} = 10$ Pa, and the heterogeneous parameter for the heterogenous foam layer was considered at a fair value of $K_n = 0.2$.

Table 3 examines the influence of the heterogeneous angle (θ) of the foam layer on the performance of the LHTES unit. The table compares the charging and discharging times for various heterogeneity angles,

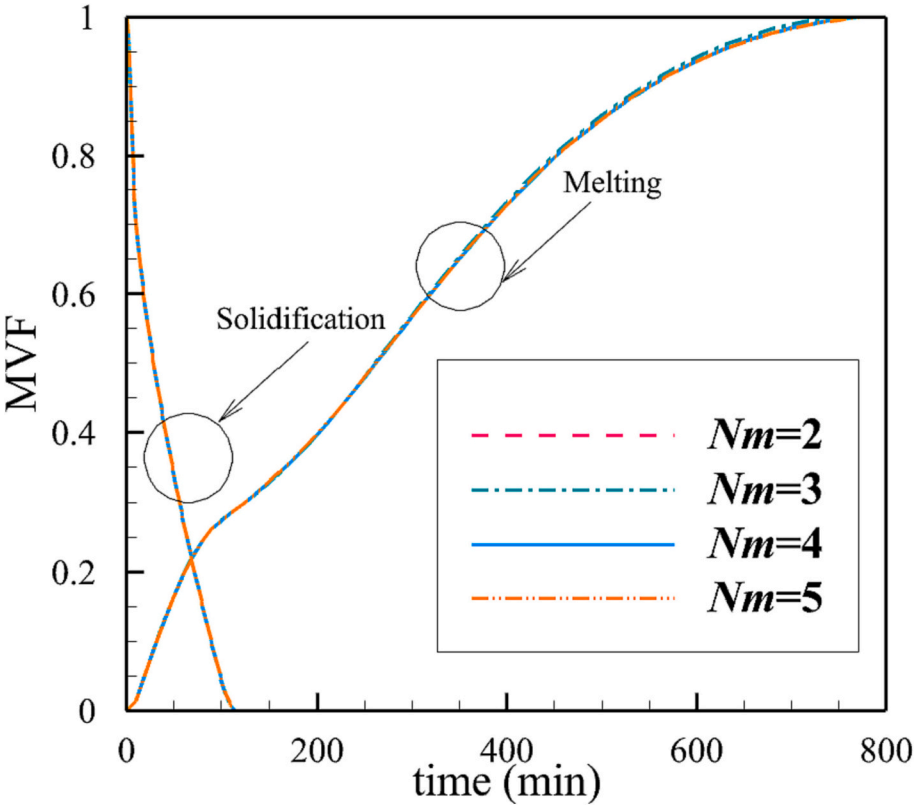

Fig. 4. Impact of mesh size on the melting volume fraction during the melting and solidification process.

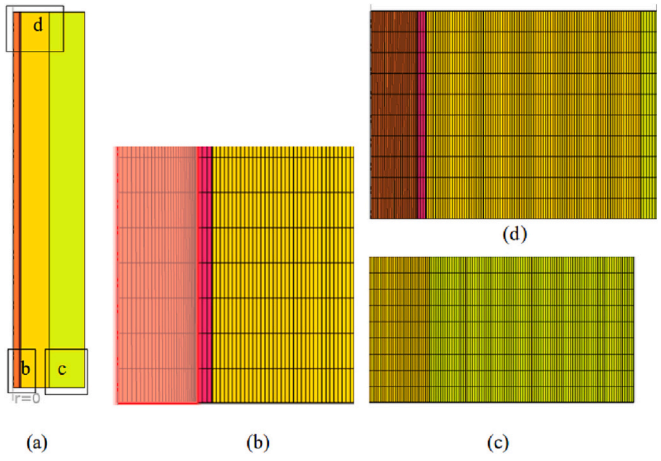

Fig. 5. An illustration of the selected, $Nm = 3$; (a): a general illustration of the model with no mesh; (b): the detailed view of the bottom section left; (c): the detailed bottom left view of the mesh; (d) the details of the mesh at the top left section.

ranging from −90° to 90°, as well as an additional case where K_n is equal to 0.

The performance of the LHTES units is assessed based on four key indicators: 90 % melting time (MVF = 0.9), 95 % melting time (MVF = 0.95), 10 % solidification time (MVF = 0.1), and 5 % solidification time (MVF = 0.05). These metrics are presented in minutes for each of the 14 cases, showcasing how the heterogeneity angle of the foam layer affects the unit's efficiency. In general, the table reveals that the charging and discharging times vary as the heterogeneous angle changes. This highlights the importance of considering the foam layer's heterogeneity angle when designing and optimizing LHTES units for improved

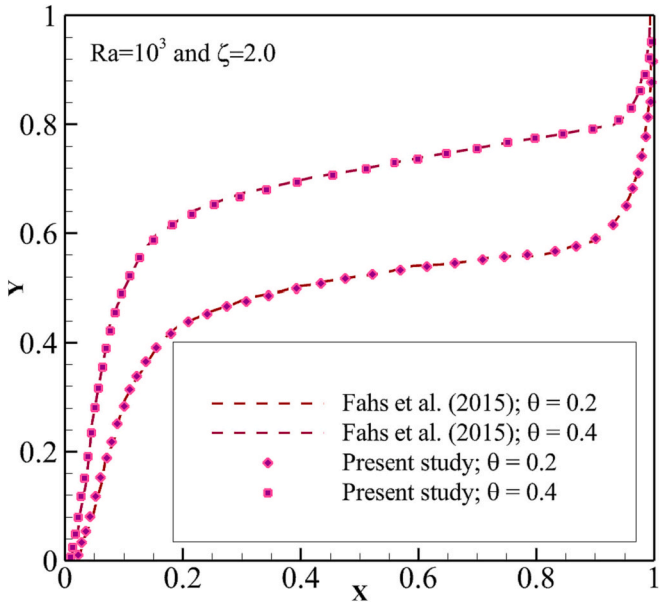

Fig. 6. An evaluation of the isotherms from [35] compared to the present calculations. The temperature curve outcomes display outstanding concurrence with previous research on natural convection within anisotropic porous materials.

performance. Further analysis of the data can provide insights into the most effective angles for specific applications, contributing to the development of more efficient energy storage systems.

Upon analyzing the data from Table 3, there is a notable trend in the melting time of 90 % with respect to the heterogeneous angle (θ) of the foam layer in the LHTES unit. Thus, the results are plotted in Fig. 9 for

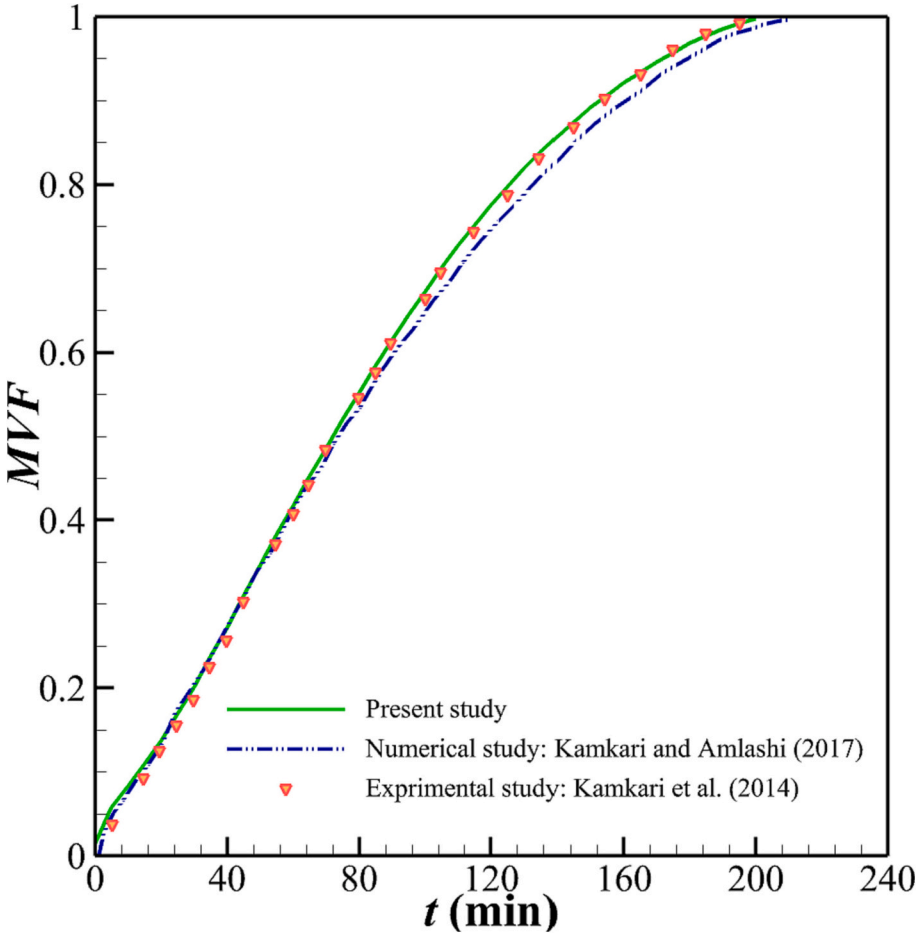

Fig. 7. Contrasting the current research with previous studies regarding MVF's relationship with time in both numerical outcomes [68] and experimental assessments [67].

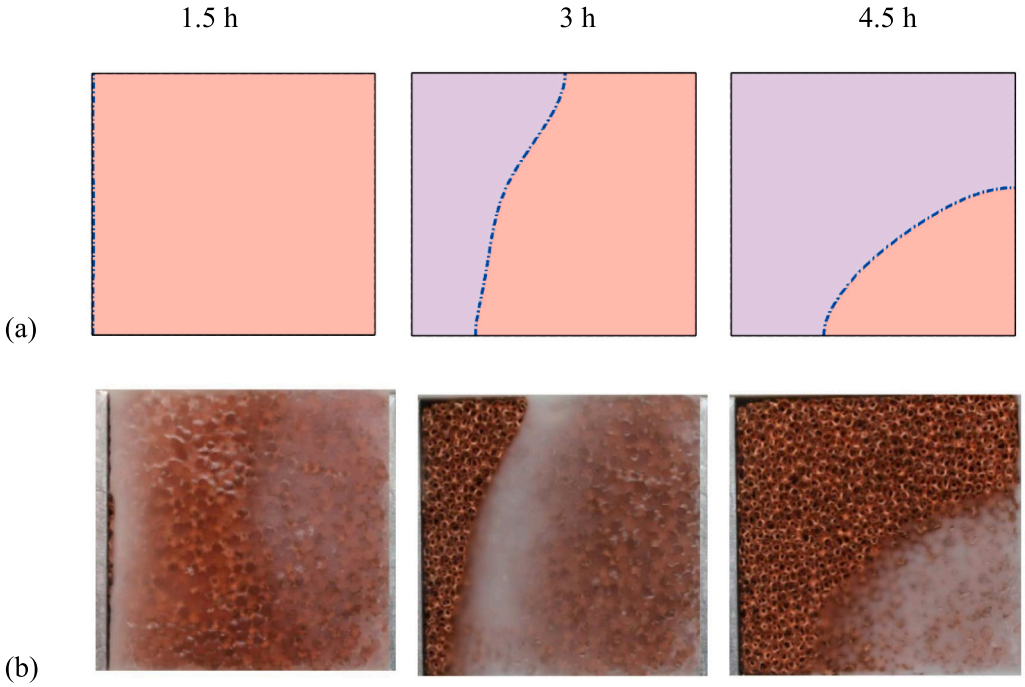

Fig. 8. The melting process of a paraffin wax-copper foam composite within a square chamber: (a) findings from the current investigation and (b) experimental data reported by [59] with permission from Elsevier.

Table 3
The charging and discharging times for various heterogenicity angles.

Cases	θ °	Melting time 90 % (min)	Melting time 95 % (min)	Solidification time 10 % (min)	Solidification time 5 % (min)
1	−90	602	682	936	1034
2	−75	594	673	932	1031
3	−60	587	660	922	1021
4	−45	571	645	911	1008
5	−30	560	632	902	998
6	−15	552	625	895	991
7	0	551	623	893	989
8	15	554	627	895	991
9	30	564	638	901	998
10	45	576	652	910	1007
11	60	590	667	922	1019
12	75	600	678	931	1030
13	90	603	681	936	1034
14	$K_n = 0$	572	646	910	1007

better analysis. As the angle (θ) increases from −90° to 0°, there is a general decrease in the 90 % melting time. This indicates that the LHTES unit charges more quickly when the heterogeneous angle approaches 0°. This trend is particularly evident between −90° and − 15°, where the melting time drops from 602 min to 552 min. However, from 0° to 90°, the 90 % melting time generally increases, suggesting that the LHTES unit takes longer to charge as the angle becomes more positive. The melting time increases from 551 min at 0° to 603 min at 90°. In summary, the 90 % melting time exhibits a trend that suggests an optimal performance near the 0° angle. The LHTES unit charges more quickly with angles closer to 0°, while more extreme positive or negative angles result in longer melting times.

Considering the solidification time of 10 % with respect to the heterogeneous angle (θ) of the foam layer, as θ increases from −90° to 0°, the 10 % solidification time generally decreases, indicating that the LHTES unit discharges more quickly when the heterogeneous angle approaches 0°. This trend is particularly evident between −90° and 0°, where the solidification time drops from 936 to 893 min. However, from 0° to 90°, the 10 % solidification time exhibits a general increase, suggesting that the LHTES unit takes longer to discharge as the angle becomes more positive. The solidification time increases from 893 min at 0° to 936 min at 90°. In summary, the 10 % solidification time shows a trend that implies optimal performance near the 0° angle. The LHTES unit discharges more quickly with angles closer to 0°, while more extreme positive or negative angles result in longer solidification times. A similar but shifted behavior can also be seen for 95 % melting and 5 % solidification curves.

Table 4 investigates the stored energy and energy release during the charging and discharging processes for various anisotropic angles (θ) of the foam layer in the LHTES unit. The table compares energy storage and releases for 14 cases with angles ranging from −90° to 90°, as well as an additional case where Kn equals 0. For each case, four key metrics are presented: ΔES at Melting 90 %, ΔES at Melting 95 %, ΔES at Solidification 10 %, and ΔES at Solidification 5 %. These values, measured in kilojoules (kJ), represent the change in stored energy through the respective melting and solidification processes.

The results in Table 4 show that the stored and released energy values are generally consistent across the range of heterogeneity angles. However, some minor variations can be observed: As the angle (θ) increases from −90° to 0°, there is a slight increase in stored energy during both the 90 % and 95 % melting processes. This indicates that the LHTES unit stores energy more efficiently as the angle approaches 0°. From 0° to 90°, the stored energy values for the 90 % and 95 % melting processes exhibit a slight decrease, implying that the LHTES unit becomes slightly less efficient in storing energy as the angle becomes more positive. In terms of energy release, the solidification ΔES values show a similar trend.

As the angle (θ) increases from −90° to 0°, the energy released during the 10 % and 5 % solidification processes becomes slightly more

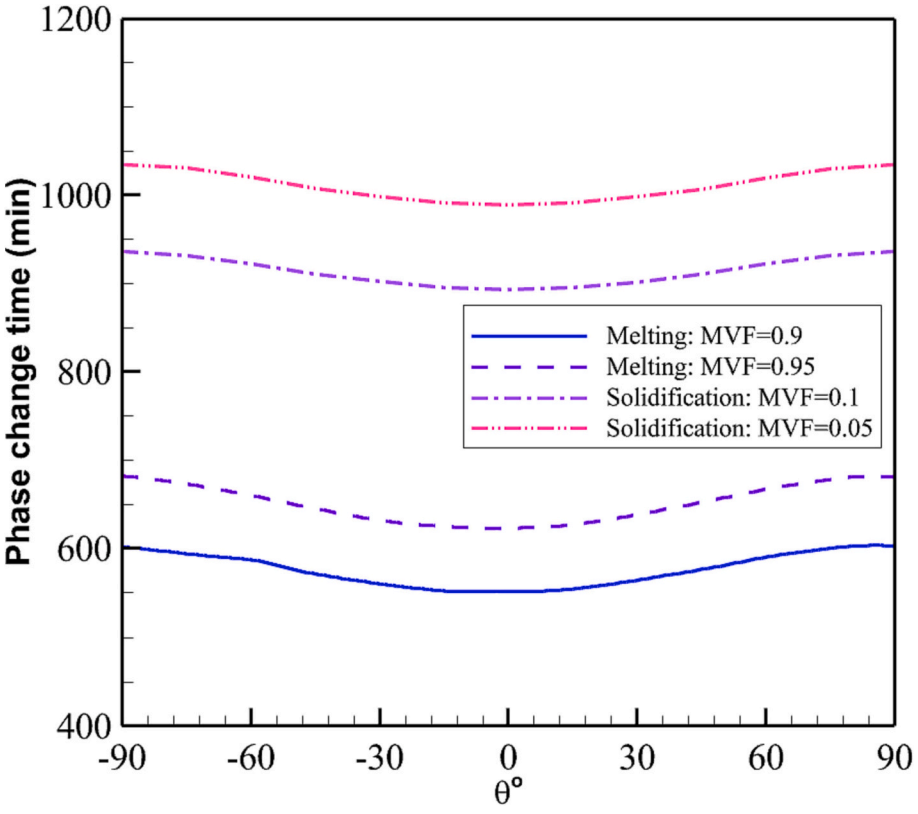

Fig. 9. A comparison of melting and solidification times for various heterogeneous angles.

Table 4
The stored energy and release during the charging and discharging processes for various heterogenicity angles.

Cases	θ °	Melting 90 % ΔES (kJ)	Melting 95 % ΔES (kJ)	Solidification 10 % ΔES (kJ)	Solidification 5 % ΔES (kJ)
1	−90	1394.2	1474.6	1325.4	1388.6
2	−75	1395.3	1475.2	1325.7	1388.9
3	−60	1396.5	1476.0	1326.2	1389.5
4	−45	1396.5	1476.7	1326.9	1390.1
5	−30	1396.3	1476.8	1327.4	1390.6
6	−15	1396.3	1477.0	1327.7	1390.9
7	0	1396.4	1477.1	1327.8	1391.0
8	15	1396.7	1477.3	1327.7	1390.8
9	30	1397.0	1477.4	1327.3	1390.4
10	45	1397.3	1477.4	1326.7	1389.8
11	60	1397.4	1477.3	1326.1	1389.2
12	75	1397.3	1477.0	1325.6	1388.7
13	90	1397.1	1476.7	1325.4	1388.6
14	$K_n = 0$	1397.1	1476.7	1326.8	1390.0

efficient. However, from 0° to 90°, the efficiency of energy release during solidification decreases slightly. In summary, the results from Table 4 suggest that the heterogeneity angle (θ) of the foam layer subtly impacts the energy storage and release competence in the LHTES, with an optimal performance near the 0° angle.

Fig. 10 displays the temporal evolution of MVF during the melting (charging) and solidification (discharging) processes for both uniform metal foam and anisotropic metal foam with anisotropic angles of θ = 0° and θ = 75°. Interestingly, an anisotropic angle of zero results in superior charging and discharging performance compared to other cases. This advantage is particularly noticeable during the middle of the phase change process, a trend that is consistent with the observations in Fig. 9.

A zero heterogeneous angle (θ) facilitates enhanced thermal conductivity toward the r direction, enabling more effective heat transmission into the PCM domain *via* the conduction mechanism. Simultaneously, it provides optimal permeability in a direction parallel to the heated surface, allowing more efficient convection flow circulation to dissipate the absorbed heat through the advection mechanism.

In the midst of the phase change process, a significant portion of the PCM is in a liquid state and influenced by the convection heat transfer mechanism. Consequently, the anisotropic angle, which alters the direction of local thermal conductivity and permeability, affects both advection and conduction mechanisms. Depending on the anisotropic angle, these mechanisms can either complement each other (at a zero angle) or undermine each other ($\theta = 75°$) when compared to a uniform metal foam without anisotropic properties.

Figs. 11 and 12 illustrate the phase interface through the melting and solidification steps at various time intervals. The results are provided for two scenarios: uniform metal foam and anisotropic metal foam with a zero anisotropic angle ($\theta = 0°$). As observed in Fig. 11, the melting process begins adjacent to the tube wall and progresses toward the interior of the enclosure.

At the initial stage ($t = 30$ min), the bottom interface is inclined more toward the PCM region. This can be attributed to heat transfer within the HTF fluid being more robust at the tube entrance, resulting in a superior heat rate at the bottom. Since the entire PCM domain is in a solid phase at the outset, there is no convection heat transfer, and the melting process is driven solely by conduction heat transfer. Consequently, the bottom melts more rapidly compared to other areas. As the melting advances, a larger portion of PCM melts, and convection mechanisms start to emerge. In a convection circulation, the heated liquid PCM adjacent to the tube wall rises and tends to expedite heat transfer at the upper regions of the enclosure. As a result, after a certain period ($t =$

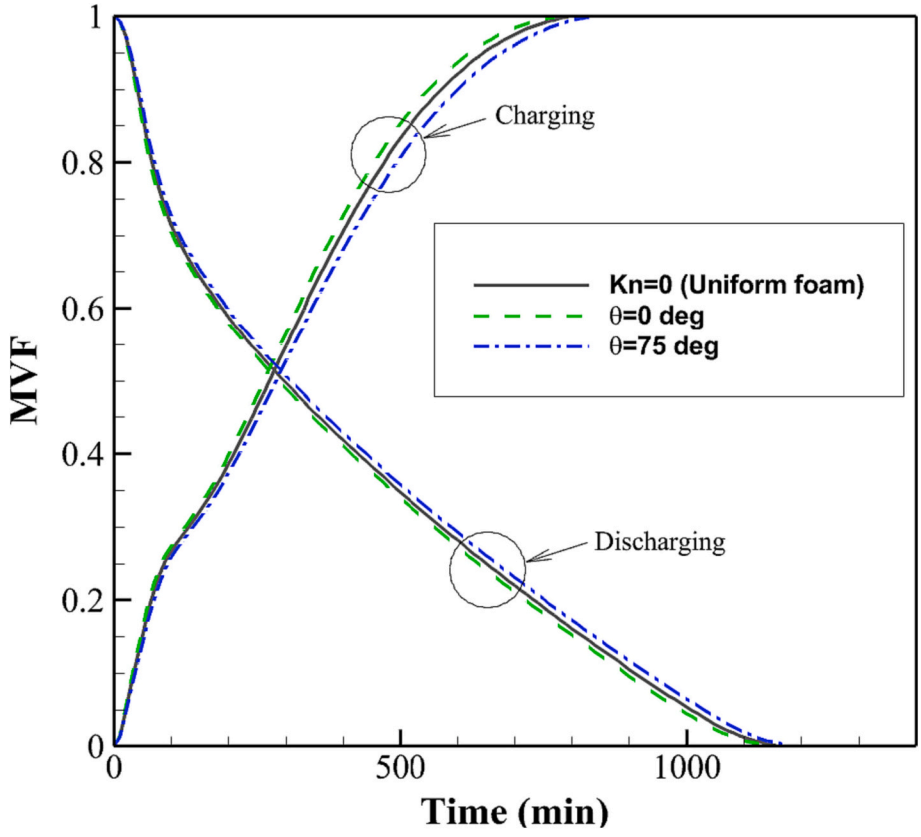

Fig. 10. Time history of MVF for various values of heterogeneous angles during the charging and discharging process. The results for uniform metal foam were added for the sake of comparison.

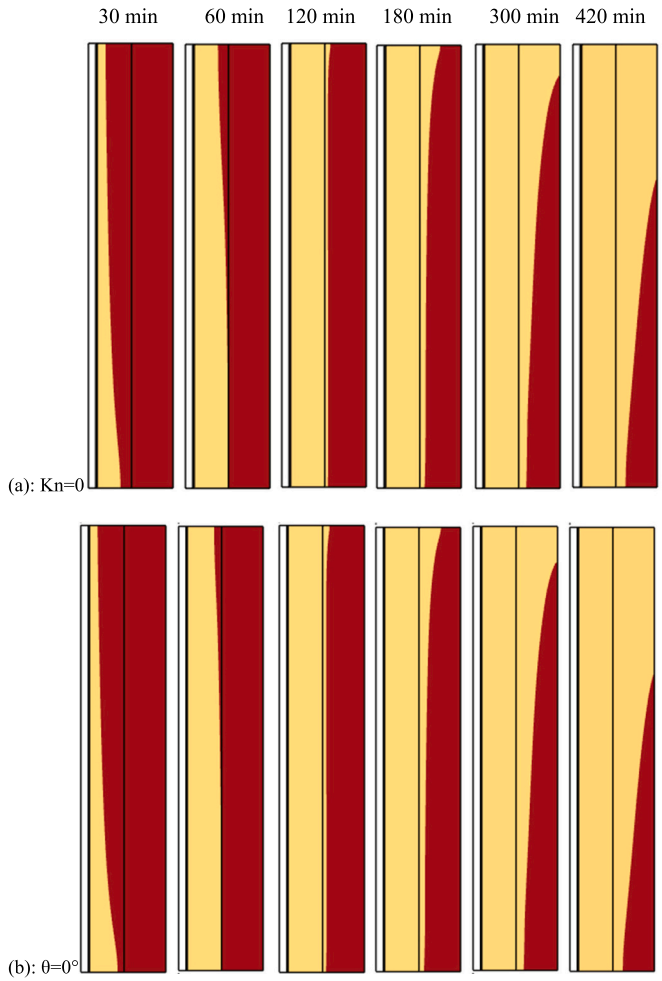

Fig. 11. A comparison of the charging process (melting) between a uniform metal foam layer and a zero-angle heterogeneous layer. (a): uniform metal foam and anisotropic meal foam with a zero anisotropic angle.

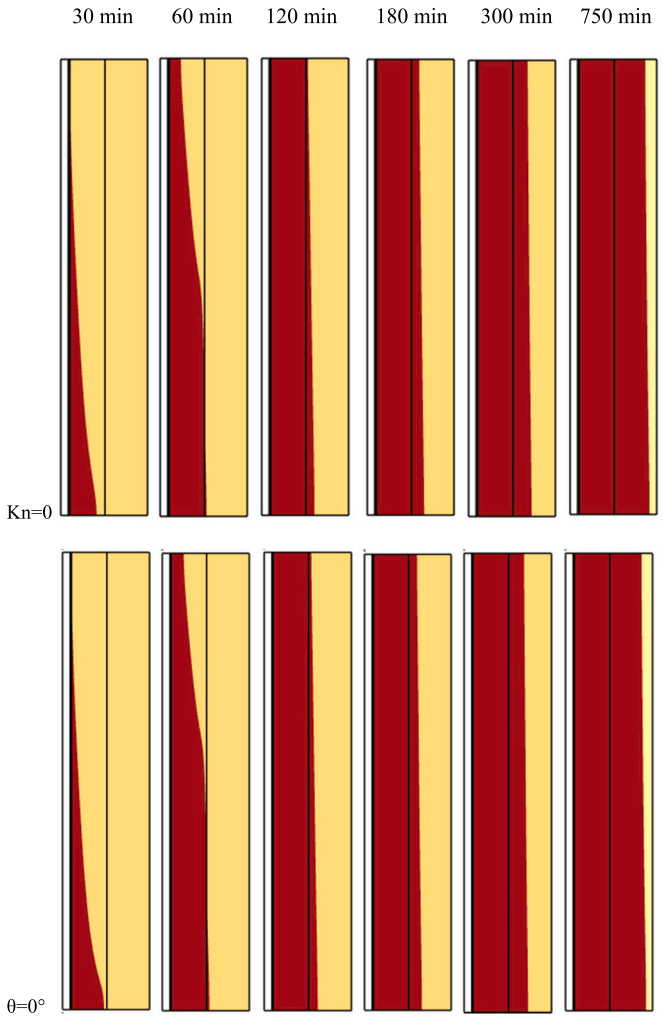

Fig. 12. A comparison of the discharging process (solidification) between a uniform metal foam layer and a zero-angle heterogeneous layer. (a): uniform metal foam and anisotropic meal foam with a zero anisotropic angle.

120 min), the melting interface at the top displays a greater inclination into the PCM domain compared to the bottom. Both uniform and anisotropic metal foam scenarios exhibit a similar behavioral trend. However, the anisotropic case demonstrates superior interface advancement compared to the uniform case.

Fig. 12 presents intriguing findings. Solidification is pronounced at the bottom of the enclosure during the initial stages due to enhanced HTF heat transfer at the entrance. Subsequently, it assumes a uniform shape within the metal foam layer. After a certain duration ($t = 180$ min), the solidification progresses uniformly, with minimal indications of a convection heat transfer mechanism, as there are negligible temperature gradients in the remaining liquid PCM.

5. Conclusions

The present work investigated the application of an anisotropic layer of metal foam in an LHTES system to improve heat transfer and thermal energy storage rates. The heterogeneous copper metal foam was integrated into a shell-tube LHTES system with paraffin wax PCM. Cases with various heterogenicity angles ranging from -90° to 90° in 15° increments were compared to a case with uniform foam. The cases are compared based on melting and solidification time, as well as the system energy response. The uniform foam case charged and discharged in 646 and 1007 min, respectively. As the heterogenicity angle became greater in the positive or negative direction, the melting and solidification time increased. Equivalent positive and negative heterogenicity angles showed similar charging and discharging times. The longest case, -90°, charged and discharged in 682 and 1034 min, respectively. The most effective case in comparison was 0° heterogenicity angle with charging and discharging times of 623 and 989 min, respectively. The uniform foam case had a change in stored energy of 1476.7 kJ and 1390.0 kJ during charging and discharging, respectively. The dissipated energy showed a similar trend to the melting and solidification time; however, the optimized stored energy was offset from 0°. The highest stored energy of 1477.4 kJ was achieved from the 30° and 40° heterogenicity angle cases, while the highest dissipated energy of 1391.0 kJ occurred at 0°. Overall, there was very little difference in the stored and dissipated energy between the cases. The proposed LHTES unit can be utilized in buildings with the aim of improving solar energy storage and enhancing efficiency of renewable energy systems.

In this study, the anisotropic layer was positioned adjacent to the heated wall. The findings indicate that the angle of anisotropy influences the outcomes. Therefore, subsequent research could focus on examining the effects of positioning an anisotropic layer near the shell wall. Additionally, future investigations might explore the effects of situating the anisotropic layer at various locations within the system, such as the bottom, middle, or top, to assess its impact on the melting behavior of the system.

CRediT authorship contribution statement

Mohamed Bouzidi: Conceptualization, Data curation, Formal analysis, Investigation, Methodology, Supervision, Writing – review & editing. **Mikhail Sheremet:** Data curation, Formal analysis, Investigation, Software, Validation, Visualization, Writing – original draft. **Kyle Shank:** Conceptualization, Formal analysis, Investigation, Writing – review & editing. **Saeed Tiari:** Conceptualization, Investigation, Supervision, Writing – review & editing. **Mohammad Ghalambaz:** Conceptualization, Data curation, Formal analysis, Investigation, Methodology, Supervision, Writing – review & editing.

Declaration of competing interest

The authors clarify that there is no conflict of interest for report.

Data availability

No data was used for the research described in the article.

Acknowledgments

This research of Mikhail Sheremet and Mohammad Ghalambaz was supported by the Tomsk State University Development Programme (Priority-2030).

References

[1] B.E. Jebasingh, A.V. Arasu, A comprehensive review on latent heat and thermal conductivity of nanoparticle dispersed phase change material for low-temperature applications, Energy Storage Mater. 24 (2020) 52–74.
[2] W. Cui, T. Si, X. Li, X. Li, L. Lu, T. Ma, Q. Wang, Heat transfer enhancement of phase change materials embedded with metal foam for thermal energy storage: a review, Renew. Sustain. Energy Rev. 169 (2022), 112912.
[3] K. Faraj, M. Khaled, J. Faraj, F. Hachem, C. Castelain, A review on phase change materials for thermal energy storage in buildings: heating and hybrid applications, J. Energy Storage 33 (2021), 101913.
[4] R. Cai, Z. Sun, H. Yu, E. Meng, J. Wang, M. Dai, Review on optimization of phase change parameters in phase change material building envelopes, J. Build. Eng. 35 (2021), 101979.
[5] M. Ghalambaz, H. Jin, A. Bagheri, O. Younis, D. Wen, Convective flow and heat transfer of nano-encapsulated phase change material (NEPCM) dispersions along a vertical surface, Facta Universitatis, Series Mech. Eng. 20 (3) (2022) 519–538.
[6] C. Ho, Y.-C. Liu, M. Ghalambaz, W.-M. Yan, Forced convection heat transfer of nano-encapsulated phase change material (NEPCM) suspension in a mini-channel heatsink, Int. J. Heat Mass Transfer 155 (2020), 119858.
[7] H. Peng, J. Wang, X. Zhang, J. Ma, T. Shen, S. Li, B. Dong, A review on synthesis, characterization and application of nanoencapsulated phase change materials for thermal energy storage systems, Appl. Therm. Eng. 185 (2021), 116326.
[8] G. Hekimoğlu, A. Sarı, A review on phase change materials (PCMs) for thermal energy storage implementations, Materials Today: Proceedings 58 (2022) 1360–1367.
[9] D. Chocontá Bernal, E. Muñoz, G. Manente, A. Sciacovelli, H. Ameli, A. Gallego-Schmid, Environmental assessment of latent heat thermal energy storage technology system with phase change material for domestic heating applications, Sustainability 13 (20) (2021) 11265.
[10] T. Xu, E.N. Humire, J.N. Chiu, S. Sawalha, Latent heat storage integration into heat pump based heating systems for energy-efficient load shifting, Energ. Conver. Manage. 236 (2021), 114042.
[11] A. Agrawal, D. Rakshit, Review on thermal performance enhancement techniques of latent heat thermal energy storage (LHTES) system for solar and waste heat recovery applications, New Research Directions in Solar Energy Technologies (2021) 411–438.
[12] M. Mohkam, S.H. Mohammadi, R. Arababadia, E. Jahanshahi Javaran, Impacts of phase change materials on performance of operational peak load shifting strategies in a sample building in hot-arid climate, Environ. Prog. Sustain. Energy 42 (1) (2022), e13961.
[13] E. Alehosseini, S.M. Jafari, Micro/nano-encapsulated phase change materials (PCMs) as emerging materials for the food industry, Trends Food Sci. Technol. 91 (2019) 116–128.
[14] S. Wu, T. Yan, Z. Kuai, W. Pan, Thermal conductivity enhancement on phase change materials for thermal energy storage: a review, Energy Storage Mater. 25 (2020) 251–295.
[15] M. Aramesh, B. Shabani, Metal foam-phase change material composites for thermal energy storage: a review of performance parameters, Renew. Sustain. Energy Rev. 155 (2022), 111919.
[16] H. Senobar, M. Aramesh, B. Shabani, Nanoparticles and metal foams for heat transfer enhancement of phase change materials: a comparative experimental study, J. Energy Storage 32 (2020), 101911.
[17] X. Huang, C. Sun, Z. Chen, Y. Han, Experimental and numerical studies on melting process of phase change materials (PCMs) embedded in open-cells metal foams, Int. J. Therm. Sci. 170 (2021), 107151.
[18] X. Wang, B. Li, Z. Qu, J. Zhang, Z. Jin, Effects of graphite microstructure evolution on the anisotropic thermal conductivity of expanded graphite/paraffin phase change materials and their thermal energy storage performance, Int. J. Heat Mass Transfer 155 (2020), 119853.
[19] M. Zhang, Q. Xiao, C. Chen, L. Li, W. Yuan, Developing a heat-insulating composite phase change material with light-to-thermal conversion performance from graphene oxide/silica hybrid aerogel, Appl. Therm. Eng. 174 (2020), 115303.
[20] Y. Qian, N. Han, X. Gao, X. Gao, W. Li, X. Zhang, Cellulose-based phase change fibres for thermal energy storage and management applications, Chem. Eng. J. 412 (2021), 128596.
[21] H. Yang, Y. Li, Y. Yang, D. Chen, Y. Zhu, Effective thermal conductivity of high porosity open-cell metal foams, Int. J. Heat Mass Transfer 147 (2020), 118974.
[22] H. Li, C. Hu, Y. He, D. Tang, K. Wang, X. Hu, Visualized-experimental investigation on the energy storage performance of PCM infiltrated in the metal foam with varying pore densities, Energy 237 (2021), 121540.
[23] M. Aramesh, B. Shabani, Metal foams application to enhance the thermal performance of phase change materials: a review of experimental studies to understand the mechanisms, J. Energy Storage 50 (2022), 104650.
[24] H.M. Ali, Heat transfer augmentation of porous media (metallic foam) and phase change material based heat sink with variable heat generations: an experimental evaluation, Sustain. Energy Technol. Assess. 52 (2022), 102218.
[25] Z. Maqbool, M. Hanief, M. Parveez, Review on performance enhancement of phase change material based heat sinks in conjugation with thermal conductivity enhancers for electronic cooling, J. Energy Storage 60 (2023), 106591.
[26] T. Wan, Y. Liu, C. Zhou, X. Chen, Y. Li, Fabrication, properties, and applications of open-cell aluminum foams: a review, J. Mater. Sci. Technol. 62 (2021) 11–24.
[27] Z.A. Raizah, S.E. Ahmed, A.M. Aly, ISPH simulations of natural convection flow in E-enclosure filled with a nanofluid including homogeneous/heterogeneous porous media and solid particles, Int. J. Heat Mass Transfer 160 (2020), 120153.
[28] N. Fajraoui, M. Fahs, A. Younes, B. Sudret, Analyzing natural convection in porous enclosure with polynomial chaos expansions: effect of thermal dispersion, anisotropic permeability and heterogeneity, Int. J. Heat Mass Transfer 115 (2017) 205–224.
[29] M. Ghalambaz, M. Aljaghtham, A.J. Chamkha, A. Abdullah, I. Mansir, M. Ghalambaz, Mathematical modeling of heterogeneous metal foams for phase-change heat transfer enhancement of latent heat thermal energy storage units, App. Math. Model. 115 (2023) 398–413.
[30] Z. Rashed, M. Alhazmi, S.E. Ahmed, Non-homogenous nanofluid model for 3D convective flow in enclosures filled with hydrodynamically and thermally heterogeneous porous media, Alex. Eng. J. 60 (3) (2021) 3119–3132.
[31] P. Maghsoudi, M. Siavashi, Application of nanofluid and optimization of pore size arrangement of heterogeneous porous media to enhance mixed convection inside a two-sided lid-driven cavity, J. Therm. Anal. Calorim. 135 (2019) 947–961.
[32] S.E. Ahmed, Z.A. Raizah, A.M. Aly, Three-dimensional flow of a power-law nanofluid within a cubic domain filled with a heat-generating and 3D-heterogeneous porous medium, Eur. Phys. J. Special Topics 230 (5) (2021) 1185–1199.
[33] Y. Zhuang, Q. Zhu, Analysis of entropy generation in combined buoyancy-Marangoni convection of power-law nanofluids in 3D heterogeneous porous media, Int. J. Heat Mass Transf. 118 (2018) 686–707.
[34] Q.Y. Zhu, Y.J. Zhuang, H.Z. Yu, Entropy generation due to three-dimensional double-diffusive convection of power-law fluids in heterogeneous porous media, Int. J. Heat Mass Transfer 106 (2017) 61–82.
[35] M. Fahs, A. Younes, A. Makradi, A reference benchmark solution for free convection in a square cavity filled with a heterogeneous porous medium, Numer. Heat Transfer Part B Fundam. 67 (5) (2015) 437–462.
[36] A. Merrikh, J. Lage, From continuum to porous–continuum: the visual resolution impact on modeling natural convection in heterogeneous media, in: Transport Phenomena in Porous Media III, Elsevier, 2005, pp. 60–96.
[37] J. Shafi, M. Ghalambaz, M. Fteiti, M. Ismael, M. Ghalambaz, Computational modeling of latent heat thermal energy storage in a shell-tube unit: using neural networks and anisotropic metal foam, Mathematics 10 (24) (2022) 4774.
[38] J.M. Mahdi, F.T. Najim, I.M. Aljubury, H.I. Mohammed, N.B. Khedher, N. K. Alshammari, A. Cairns, P. Talebizadehsardari, Intensifying the thermal response of PCM via fin-assisted foam strips in the shell-and-tube heat storage system, J. Energy Storage 45 (2022), 103733.
[39] K. Nedjem, A. Laouer, M. Teggar, E.H. Mezaache, M. Arıcı, K.A. Ismail, Performance enhancement of triplex tube latent heat storage using fins, metal foam and nanoparticles, Int. Commun. Heat Mass Transfer 139 (2022), 106437.
[40] V. Joshi, M.K. Rathod, Experimental and numerical assessments of thermal transport in fins and metal foam infused latent heat thermal energy storage systems: a comparative evaluation, Appl. Therm. Eng. 178 (2020), 115518.
[41] X. Yang, P. Wei, X. Wang, Y.-L. He, Gradient design of pore parameters on the melting process in a thermal energy storage unit filled with open-cell metal foam, Appl. Energy 268 (2020), 115019.
[42] C. Zhao, M. Opolot, M. Liu, F. Bruno, S. Mancin, K. Hooman, Phase change behaviour study of PCM tanks partially filled with graphite foam, Appl. Therm. Eng. 196 (2021), 117313.
[43] V. Joshi, M.K. Rathod, Thermal performance augmentation of metal foam infused phase change material using a partial filling strategy: an evaluation for fill height ratio and porosity, Appl. Energy 253 (2019), 113621.

[44] S. Christopher, K. Parham, A. Mosaffa, M. Farid, Z. Ma, A.K. Thakur, H. Xu, R. Saidur, A critical review on phase change material energy storage systems with cascaded configurations, J. Clean. Prod. 283 (2021), 124653.
[45] H. Wang, Z. Liu, H. Wu, Entransy dissipation-based thermal resistance optimization of slab LHTES system with multiple PCMs arranged in a 2D array, Energy 138 (2017) 739–751.
[46] S. Zhang, Y. Yao, Y. Jin, Z. Shang, Y. Yan, Heat transfer characteristics of ceramic foam/molten salt composite phase change material (CPCM) for medium-temperature thermal energy storage, Int. J. Heat Mass Transfer 196 (2022), 123262.
[47] M. Ghalambaz, A.A. Melaibari, A.J. Chamkha, O. Younis, M. Sheremet, Phase change heat transfer and energy storage in a wavy-tube thermal storage unit filled with a nano-enhanced phase change material and metal foams, J. Energy Storage 54 (2022), 105277.
[48] D.A. Nield, A. Bejan, Convection in Porous Media, Springer, 2006.
[49] Y. Yao, H. Wu, Interfacial heat transfer in metal foam porous media (MFPM) under steady thermal conduction condition and extension of Lemlich foam conductivity theory, Int. J. Heat Mass Transfer 169 (2021), 120974.
[50] C. Zhao, J. Wang, Y. Sun, S. He, K. Hooman, Fin design optimization to enhance PCM melting rate inside a rectangular enclosure, Appl. Energy 321 (2022), 119368.
[51] M. Iasiello, N. Bianco, W.K. Chiu, V. Naso, Anisotropic convective heat transfer in open-cell metal foams: assessment and correlations, Int. J. Heat Mass Transfer 154 (2020), 119682.
[52] M. Ghalambaz, M. Aljaghtham, A.J. Chamkha, A. Abdullah, A. Alshehri, M. Ghalambaz, An anisotropic metal foam design for improved latent heat thermal energy storage in a tilted enclosure, Int. J. Mech. Sci. 107830 (2022).
[53] Y. Yao, H. Wu, Macroscale modeling of solid–liquid phase change in metal foam/paraffin composite: effects of paraffin density treatment, thermal dispersion, and interstitial heat transfer, J. Therm. Sci. Eng. Applic. 13 (4) (2021).
[54] Y. Yao, H. Wu, Z. Liu, Direct simulation of interstitial heat transfer coefficient between paraffin and high porosity open-cell metal foam, J. Heat Transfer 140 (3) (2018).
[55] A.I.N. Korti, H. Guellil, Experimental study of the effect of inclination angle on the paraffin melting process in a square cavity, J. Energy Storage 32 (2020), 101726.
[56] A. Agarwal, R. Sarviya, Characterization of commercial grade paraffin wax as latent heat storage material for solar dryers, Mater. Today: Proc. 4 (2) (2017) 779–789.
[57] N. Ukrainczyk, S. Kurajica, J. Šipušić, Thermophysical comparison of five commercial paraffin waxes as latent heat storage materials, Chem. Biochem. Eng. Q. 24 (2) (2010) 129–137.
[58] S.-K. Choi, S.-O. Kim, T.-H. Lee, Dohee-Hahn, computation of the natural convection of nanofluid in a square cavity with homogeneous and nonhomogeneous models, Numer. Heat Transfer Part A Appl. 65 (4) (2014) 287–301.
[59] H. Zheng, C. Wang, Q. Liu, Z. Tian, X. Fan, Thermal performance of copper foam/paraffin composite phase change material, Energ. Conver. Manage. 157 (2018) 372–381.
[60] O.C. Zienkiewicz, R.L. Taylor, P. Nithiarasu, The Finite Element Method for Fluid Dynamics, Seventh Edition ed, Butterworth-Heinemann, Oxford, 2014.
[61] D. Pepper, The Intermediate Finite Element Method: Fluid Flow and Heat Transfer Applications, Routledge, 2017.
[62] C.T. Kelley, Solving Nonlinear Equations with Newton's Method, SIAM, 2003.
[63] P. Deuflhard, Newton Methods for Nonlinear Problems: Affine Invariance and Adaptive Algorithms, Springer Science & Business Media, 2005.
[64] M. Bollhöfer, O. Schenk, R. Janalik, S. Hamm, K. Gullapalli, State-of-the-art sparse direct solvers, in: Parallel Algorithms in Computational Science and Engineering, 2020, pp. 3–33.
[65] M. Bollhöfer, A. Eftekhari, S. Scheidegger, O. Schenk, Large-scale sparse inverse covariance matrix estimation, SIAM J. Sci. Comput. 41 (1) (2019) A380–A401.
[66] G. Söderlind, L. Wang, Adaptive time-stepping and computational stability, J. Comput. Appl. Math. 185 (2) (2006) 225–243.
[67] B. Kamkari, H. Shokouhmand, F. Bruno, Experimental investigation of the effect of inclination angle on convection-driven melting of phase change material in a rectangular enclosure, Int. J. Heat Mass Transfer 72 (2014) 186–200.
[68] B. Kamkari, H.J. Amlashi, Numerical simulation and experimental verification of constrained melting of phase change material in inclined rectangular enclosures, Int. Commun. Heat Mass Transfer 88 (2017) 211–219.